JOURNAL OF MATERIALS SCIENCE 33 (1998) 2965–2973

# Finite element study of the fibre–matrix interface behaviour of [10°/90°] laminated composites under tensile loading

H. MAHFUZ, A. K. M. A. MIAN, U. VAIDYA, T. BROWN, S. JEELANI
*Tuskegee University's Center for Advanced Materials, Tuskegee, AL 36088, USA*
*E-mail: ememah@acd.tusk.edu*

A three-dimensional unit cell has been developed and modelled using the finite element method to investigate the interface failure behaviour of $SiC_f/Si_3N_4$ composites under tensile loading at room and elevated temperatures. The model idealizes the composite as a regular rectangular array of fibres in 0° and 90° orientations embedded in the matrix. It introduces three-dimensional contact elements between the fibre and the matrix to simulate the interface conditions between the two phases. Slippage between 0° and 90° layers is also considered by introducing another set of contact elements at the layer separation planes. Two interface conditions, namely, infinitely strong and weakly bonded, are considered to establish the correlation with the experimental data. To simulate the weak interface, the fibre and the matrix are assumed to slide over one another with shear stress through the Coulomb mechanism. The same assumption has been adopted for the layer separation planes. A finite element model utilizing these concepts has been developed. Stress–strain behaviour and the local stress distributions at various ambient temperatures within the unit cell, are presented. The investigation has also been extended to include the effects of residual stresses in the finite element model. It is shown that the model yields results that correlated reasonably well with the experimental data. 

## 1. Introduction

Composites are mainly made of fibres embedded in a matrix with lower stiffness and strength, and are very popular due to their high strength to weight ratio. The orientation of the fibre is chosen in such a way that it suites the direction of external load. Among the composite families, ceramic fibre reinforced ceramic matrix composites (CFCMC) are being used in aerospace and military structures due to their high-temperature resistance ($> 1000\,^{\circ}C$) and high modulus [1]. Continuous fibre CFCMCs are of particular interest, due to their higher damage tolerance and less-brittle failure behaviour, compared to the monolithic ceramic counterpart [2, 3]. The principal objectives of the processing of ceramic fibre-reinforced composites have been to enhance the toughness and the strain to failure [4]. It is generally accepted that the toughening of CFCMCs occurs primarily through the fibre pull-out mechanism [5, 6]. In this fibre pull-out mechanism, the strength of the fibre–matrix interface is very important. Also, the fibre–matrix interface strength is one of the key parameters responsible for the stress–strain behaviour and damage tolerance of ceramic composites [7]. Owing to the anisotropy of the composite materials, it is almost impossible to avoid induced transverse shear which may lead to premature failure of the laminate [8, 9]. Accurate knowledge of those stresses, especially at the fibre–matrix interface, is particularly important to predict the interface failure and the eventual failure of the laminate [10]. The strain to failure of the composites also depends on the interface condition of the material. The interface characterizes the mode of crack growth within the composite. Weak interface deflects the crack at the interface along the fibre length, thereby delaying the ultimate failure, called progressive failure, whereas for the strong interface, the crack penetrates the fibre while growing through the matrix causing catastrophic failure. The prediction of the performance of this interface with respect to an external loading is, therefore, important, and is necessary to visualize the failure of the laminate.

Most recently, the interface condition has been extensively studied and discussed within the context of its effect upon toughness and energy dissipation during the fracture process. All these works have been performed under transverse load, i.e. load is applied perpendicular to the fibre direction. Therefore, it is possible in these cases to model the interface using a two-dimensional model as opposed to the present situation. Owing to the external tensile loading along the fibre axis direction, the present model essentially assumes a three-dimensional form. Literature search reveals that no work has been done in the modelling of

0°/90° laminated composites. The bonding strength of the layer separation planes also plays an important role in the composite failure mechanisms, especially in the delamination of the laminate. If the matrix is well bonded at layer separation planes, the interlaminar shear stress will be comparatively higher. As of now, none of the models available in literature considers the layer separation planes.

Pluvinage and Quenisset [11] developed a numerical tool in order to predict the influence of the main processing parameters on the mechanical behaviour of 0/90°C laminated SiC/SiC composites. The two-dimensional model proposed by them represented the various features and sequences of laminate damage behaviour. Folias [9], on the other hand, developed a three-dimensional model for uniaxial composites under transverse tensile load. The strain energy release rate was computed and the criterion was used to predict debond initiation at the fibre–matrix interface. The failure was most likely to occur at the free surface, i.e. the region where the fibre intersects a free surface, for example, a hole, an edge, or a crack.

In order to characterize the time-dependent behaviour of composites of various fibre–matrix combinations, a micro-mechanical model was developed by Schaffer and Adams [12]. The analysis used a finite element model capable of simulating a unidirectional composite subjected to a combination of longitudinal and transverse loading, as well as hygrothermal loading. Time-dependent non-linear (elastoplastic) material behaviour was included in the analysis. Cartian and Gibson [13] studied the damping characteristics of composites using special fibre coatings, thereby modifying the interface conditions. Both two- and three-dimensional finite element models were developed in order to compare the influence of plane stress and plane strain conditions on the damping and the stiffness properties of the composite micro-mechanical model. The applied load was again transverse to the fibre direction while they assumed a well-bonded interface condition. The authors concluded that coating applied to the fibre modifies stress distribution, strain energy, and the elastic properties of the composite structure. A common assumption in all the above investigations is to ignore the effects of process-induced residual stresses.

In contrast to previous studies, very few investigations have been performed taking the residual stress under consideration which is invariably induced in a composite during the curing process. Nimmer [14] presented a micro-mechanical model which focused on the effects of interface conditions on transverse stress–strain behaviour of the composite. The model considered the effect of thermally induced residual stress. A considerable amount of radial compressive stress was observed at the interface due to cooling down of the unit cell from high temperature to room temperature. The investigation was undertaken considering both strong and weak interface conditions. For the weak interface condition, the effect of the friction factor on the stress–strain response of the composite was studied and no significant effect was observed. Nimmer *et al.* [15] also developed a model similar to their previous one [14]. They considered both strong and weak interface conditions, and the investigations were performed at room and elevated temperatures. For the weak interface condition, the coefficient of friction at the interface was 0.3 to account for the interface shear. The data obtained from strong and weak interface models were compared with the experimental results. Povirk and Needleman [16] simulated the fibre pull-out using finite element methods. They also simulated the residual stresses that developed while cooling down the cylinder from its processing temperature. Although the load was applied along the fibre axis, their model was again two-dimensional. The interface between the fibre and the matrix was characterized in terms of a rate-dependent internal variable friction constitutive relation.

In the current investigation, a three-dimensional unit cell has been developed for 0°/90° laminated ceramic matrix composites ($SiC_f/Si_3N_4$), and the model is incorporated into a finite element programme. The analysis also accounts for the residual stresses and slippage at the layer separation planes. Finite element predictions have been correlated with the experimental results and optical micrographs.

## 2. Materials

$SiC_f/Si_3N_4$ composite specimens, manufactured by Textron Speciality Materials, were used in the experimental work. The material has 0°/90° lay-up sequence with the density of 3.86 gm/cm$^{-3}$. The fibre is SiC with a double carbon-rich layer on the outside surface and has a diameter of 140 μm. The fibres were produced by a high-temperature vapour deposition process using carbon monofilament as a substrate. The matrix is $Si_3N_4$ with 1.5% MgO, 5% $Y_2O_3$ and 1.0% $Al_2O_3$ used as sintering aids. The $SiC_f/Si_3N_4$ composites were fabricated from suspensions of $Si_3N_4$ powder which were applied around collimated continuous SiC fibres. The green preform or tape lay-up was assembled in graphite dies and hot pressed to consolidate the matrix. The fibre volume fraction of the composite obtained by the process was about 0.3.

## 3. Finite element model

### 3.1. Element formulation

The fibre and matrix of the composite have been modelled separately using eight-noded isoparametric solid elements available in the commercial ANSYS code. The element used in the model had three degrees of freedom at each node, namely, translations in the $x$, $y$, and $z$ directions. The element also had plasticity, creep, swelling, stress stiffening, large deflection, and large strain capabilities. For the weak interface condition, the interface and layer separation planes were modelled with five-noded contact elements. This element was used to represent contact and sliding between the two surfaces. The combined mechanism of structural contact and thermal contact was modelled by the contact elements. As shown in Fig. 1, two potential contact surfaces are referred to as either the "target surface" or the "contact surface" [17]. The

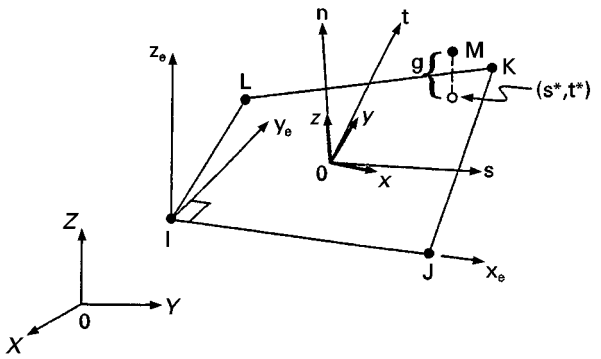


*Figure 1* Contact element with target nodes.

target surface is represented by target nodes I, J, K and L, and the contact surface node is represented by the contact node M. In general, the contact occurs when the contact node penetrates the target base. In our case, the contact node was placed in the matrix, while the target base was on the fibre. Both elastic Coulomb friction and rigid Coulomb friction were allowed, and sliding was considered only along the target base.

The finite element formulations for the isoparametric solid elements are well known, and can be found in any standard finite element text book and also in Kohnke [17]. However, the consideration of residual stress and weak interface in the FEM analysis is not trivial, and therefore, a brief description of their formulations are presented below.

### 3.1.1. Model without residual stresses

The stiffness matrix for the isoparametric solid element can be written as [18, 19]

$$[K_1] = \int_{vol_1} [B]^{\mathrm{T}} [D] [B] \, \mathrm{d}(vol)_1 \tag{1}$$

where $[B]$ is the strain-displacement matrix, $[D]$ is the stress–strain matrix and $vol_1$ is the original volume of the element. Formulations for $[B]$ and $[D]$ matrices can be found in the above references. Because the element is isoparametric, the temperature distribution was also assumed to vary with the shape function of the element. The thermal strain due to the temperature change is [17]

$$\{\varepsilon^{\mathrm{th}}\} = \{\alpha\} (\{N\}^{\mathrm{T}} \{T\} - T_{\mathrm{ref}}) \tag{2}$$

where $\{N\}$ is the shape function matrix, $\{\alpha\}$ the coefficient of thermal expansion, $\{T\}$ the nodal temperature and $T_{\mathrm{ref}}$ reference temperature.

The nodal load vector due to the change in temperature can now be written as [17]

$$\{F_1^{\mathrm{th}}\} = \int_{vol_1} [B]^{\mathrm{T}} [D] \{\varepsilon^{\mathrm{th}}\} \, \mathrm{d}(vol)_1 \tag{3}$$

If the element is now loaded with traction and thermal load simultaneously, i.e. if the material is being heated up and, at the same time, some external load is being applied, the load–displacement relationship can be expressed as

$$\{F^{\mathrm{pr}}\} + \{F_1^{\mathrm{th}}\} = [K_1] \{u\} \tag{4}$$

where $\{u\}$ is the resultant displacement matrix measured from the original shape of the element, and $\{F^{\mathrm{pr}}\}$ is the nodal load vector due to traction.

The matrix $[K_1]$ is obtained from Equation 1 and the solution of Equation 4 yields the displacement field $\{u\}$.

### 3.1.2. Formulation considering residual stresses

To model the effect of residual stresses due to the cooling down from the process temperature to room temperature, thermal load was first applied to the element and the initial stiffness matrix was obtained. The stiffness matrix and the nodal load vector due to the cool down process are the same as described before, except that $(\{T\} - T_{\mathrm{ref}})$ would now be a negative quantity. The displacement matrix can now be found from

$$\{\varepsilon^{\mathrm{th}}\} = [B] \{u_1\} \tag{5}$$

where $u_1$ is the displacement of the model due to the thermal load alone. $\{\varepsilon^{\mathrm{th}}\}$ is calculated from Equation 2. The displaced model (thermally loaded) is next loaded with surface traction corresponding to the external mechanical load. Owing to the cooling down, the volume of the element will change. If the changed volume is $(vol)_2$, the nodal load vector $\{F_2^{\mathrm{th}}\}$ due to the initial thermal load can be written as

$$\{F_2^{\mathrm{th}}\} = \int_{vol_1} [B]^{\mathrm{T}} [D] \{\varepsilon^{\mathrm{th}}\} \, \mathrm{d}(vol)_2 \tag{6}$$

and the new stiffness matrix will be

$$\{K_2\} = \int_{vol_1} [B]^{\mathrm{T}} [D] [B] \, \mathrm{d}(vol)_2 \tag{7}$$

The load–displacement relationship is then

$$[F^{\mathrm{pr}}\} + \{F_1^{\mathrm{th}}\} + \{F_2^{\mathrm{th}}\} = [K_2] \{u - u_1\} \tag{8}$$

Solution of Equation 8 yields the displacement field of the model with residual stress.

### 3.1.3. Weak interface

As mentioned earlier, contact elements were used to model the interface and layer separation planes for the weak interface condition. The tangential stiffness matrix for this element is [17]:

for sticking contact

$$[K] = K_{\mathrm{n}} \{N_{\mathrm{n}}\} \{N_{\mathrm{n}}\}^{\mathrm{T}} + K_{\mathrm{S}} (\{N_x\} \{N_x\}^{\mathrm{T}} + \{N_y\} \{N_y\}^{\mathrm{T}}) \tag{9}$$

and for sliding contact

$$[K] = K_{\mathrm{n}} \{N_{\mathrm{n}}\} \{N_{\mathrm{n}}\}^{\mathrm{T}}$$

where, $K_n$ is the stiffness of the contact surface and $N$s are the interpolation vectors. These interpolation vectors are defined in terms of the local $s$–$t$ coordinates and evaluated at the point of projection ($s = s^*, t = t^*$) of the contact node M to the target plane I–J–K–L as shown in Fig. 1.

## 3.2. Model development

The composite laminate with 0°/90° lay-up sequence is represented by a three-dimensional element as shown in Fig. 2. Owing to the loading condition and fibre orientation, the unit cell is a natural offspring of an infinite, regular and rectangular array of fibres embedded in the matrix. This style of idealization has often been used to study composite micromechanics [12–16, 20]. But all those idealizations were simplified to a two-dimensional problem as the laminate consisted of 0° layers only. The expanded view of the three-dimensional unit cell is shown in Fig. 3. The dimensions of the unit cell, i.e $B$, $L$, and $C$ (Fig. 3), are calculated from the laminate configuration and from the fibre volume fraction, $v_f$. If $n$ is the number of layers, $d_f$ the fibre diameter, and $h$ the laminate thickness, then

$$C = \frac{h}{2n} \tag{10a}$$

$$B = \frac{n\pi d_f^2}{8hv_f} \tag{10b}$$

The length $L$ of the unit cell is taken equal to $B$ to be consistent with the geometry of the unit cell. The fibre and the matrix were modelled with three-dimensional, eight-noded isoparametric solid elements with three degrees of freedom at each node. Symmetry boundary conditions have been applied at the faces $X = 0$, $Y = 0$ and $Z = 0$. These symmetry conditions are such that the translations have no component normal to the plane of symmetry. In other words, at the face $X = 0$, displacement $u$ is constrained while displacements $v$ and $w$ are free so that thermal and Poisson's effects can take place in the $Y$ and $Z$ directions in that face. The case with the face at $Y = 0$ is similar, except that $v$ is constrained at this time, and $u$ and $w$ are free. The face at $Z = 0$ follows the similar pattern of restrictions. It is also to be noted that three faces opposite to these symmetry planes are free from any restrictions except the face at $X = B$, where the load is being applied. Load is applied at face $X = B$ as distributed load using a pressure card with the restriction that nodes on this face can only move in the $X$-direction.

Two interface conditions, namely weak and strong were considered in this investigation. In the case of the strong interface, the finite element model employs a common set of nodes along the interface to describe both matrix and fibre elements. There are no interface boundary conditions associated with this model. A five-noded, three-dimensional gap element was used for modelling the interface and layer separation planes. In the weak interface case, the matrix and fibre portions of the finite element model have separate and independent element nodes, and the associated degrees of freedom are along the interface. At the interface, local fibre and matrix surfaces can slide over one another. During this sliding, shear forces parallel to the interface are transferred from the fibre to the matrix according to Coulomb's law; however, tensile stresses perpendicular to the interface are not allowed.

Similar boundary conditions for the gap elements were also applied in the layer separation planes. The concept of using an interface element at the layer separation plane traces back to the construction of the laminate using the hot-pressing technique. Although the matrix has been consolidated and cured, the effects of the layer separation plane will still be there. Even in composites that are fabricated through liquid injection moulding (non-pre-preg) where free flow of resins takes place between the preforms, the layer separation planes become important during the failure of the laminate. Because of this layer separation, transverse strain is discontinuous through the thickness of the

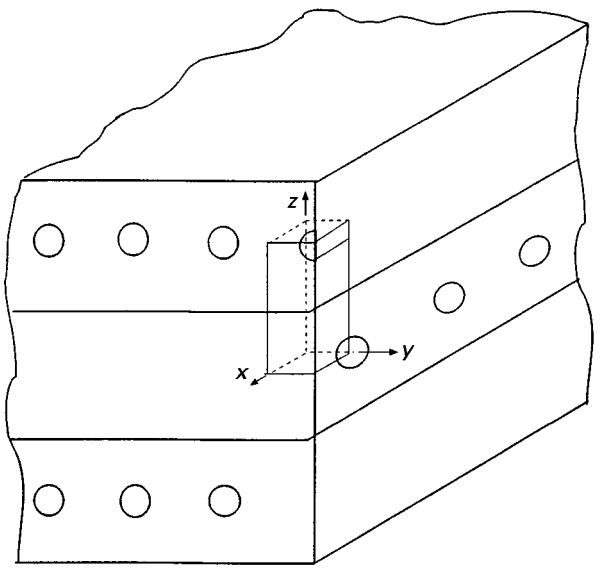


*Figure 2* Infinite array of fibres.

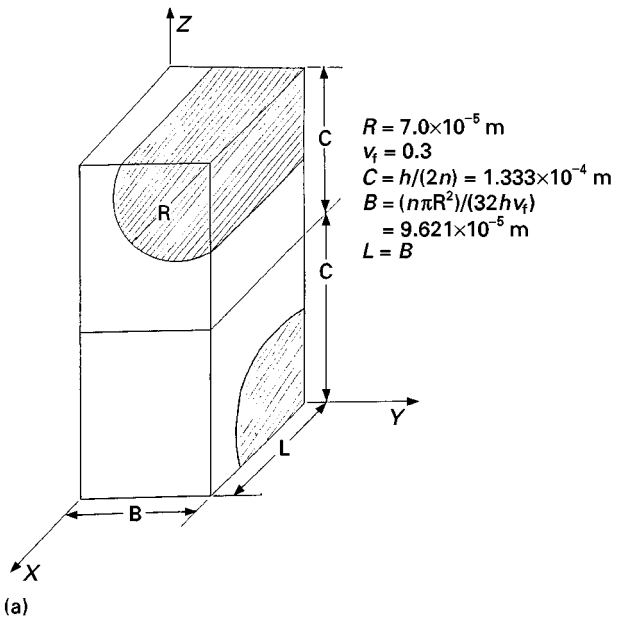


*Figure 3a* Unit cell for finite element analysis.

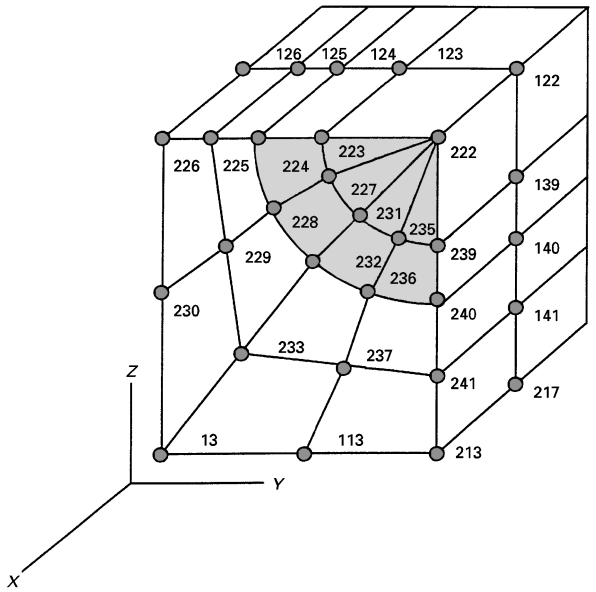


| Node # | x-Displacement $u_x(\times 10^{-3}$ mm) |
|---|---|
| 122 | − 0.134 |
| 123 | − 0.0516 |
| 124 | 0.0412 |
| 125 | 0.112 |
| 126 | 0.152 |
| 139 | − 0.018 |
| 140 | 0.108 |
| 141 | 0.649 |
| 217 | 0.949 |
| 222 | − 0.1803 |
| 223 | − 0.0695 |
| 224 | 0.0762 |
| 225 | 0.726 |
| 226 | 0.816 |
| 227 | − 0.0042 |
| 228 | 0.2064 |
| 229 | 1.38 |
| 230 | 1.84 |
| 231 | 0.0251 |
| 232 | 0.268 |
| 233 | 2.15 |
| 13 | 2.33 |
| 235 | 0.0192 |
| 236 | 0.26 |
| 237 | 1.97 |
| 113 | 2.28 |
| 239 | − 0.0226 |
| 240 | 0.175 |
| 241 | 1.60 |
| 213 | 1.90 |

*Figure 3b* X-Displacement of the nodes corresponding to the upper half of the model (RT, strong interface, without residual stress).

laminate. The physical separation between the two layers across the layer-separation planes can cause delamination which, in turn, can reduce the strength and stiffness significantly. The slippage or separation of the planes may occur due to interlaminar shear and interlaminar tensile stresses which usually stem from the anisotropy of the laminate. Triggered by the initial matrix crack or by interface debonding, delamination is one of the major failure modes for composites, and it is only confined within the layer-separation plane. At any other point in the matrix, for example somewhere in the preform, delamination cannot occur due to the presence of the fibre. The layer-separation plane is, therefore, a critical plane, and has been investigated in this study by introducing gap elements.

The friction factor used in this investigation was 0.3, and the initial gap was taken to be zero for the gap element.

For both interface conditions, the effects of residual stresses were also considered. To model this cool-down process as stated previously, thermal load was applied at the beginning, which yielded stress–strain solutions due to the cooling of the composite from 1700 °C to room temperature (RT). Later mechanical loads were applied at three temperatures, namely, RT, 800 and 1600 °C to obtain $\{u - u_1\}$ so that the final solution of $\{u\}$ included the cooling-down effect. The stiffness matrix obtained due to the initial thermal load is updated during the later steps with the application of external mechanical load to generate the overall stiffness matrix for the FEM solution.

Both large displacement and plastic strain behaviour of the material have been considered to account for geometric and material non-linearities. Linear stress–strain behaviour for the fibre and, on the other hand, non-linear and temperature-dependent stress–strain behaviour for the matrix, have been considered. The material non-linearities for the matrix have been implemented by a set of data points on the bilinear elastic curve. The initial modulii for fibre and matrix at RT were 410 and 7.21 GPa, respectively. The coefficient of thermal expansion was taken as $2.3 \times 10^{-6}$ and $4.0 \times 10^{-6}$ °C$^{-1}$ for fibre and matrix, respectively.

## 4. Results and discussion

The following discussions mainly focus on the fibre-matrix interface failure at RT (23 °C), 800 and 1600 °C under tensile loading. The analysis is based on finite element output and its correlation with the experimental results. Post-failure analysis has also been performed through scanning electron microscopy (SEM), and the micrographs of the interfacial failures are presented and discussed to complement the FEM analysis.

### 4.1. Without residual stress

Figs 4 and 5 illustrate the average stress–strain response of the unit cell at RT and 1600 °C, respectively. The average longitudinal stress is taken as the applied tensile stress during the experimental test. The longitudinal strain is defined as the ratio of the maximum displacement of the loaded face to the length, $L$, of the unit cell. It is noted at Fig. 3b that the displacement values are different in the matrix and the fibre. The maximum displacement was observed in the matrix, and the strain was calculated based on that displacement. FEM results with strong and weak interfaces are compared with the experimental data in Figs 4 and 5. It is observed that correlation between experimental and FEM results with a strong interface is quite reasonable at both temperatures. In both the cases, the correlation is better at the initial stage and diverges slightly at higher stress level. However, the correlation between the experimental and FEM results for weak interface conditions, as shown in Figs 4 and 5, is not as good. This indicates that the interface conditions, namely, the friction factor and the contact stiffness in the analysis, are not an accurate representation of the actual interface.

Contours of the longitudinal stress $\sigma_x$, at RT and 800 °C for strong interface are shown in Figs 6 and 7,

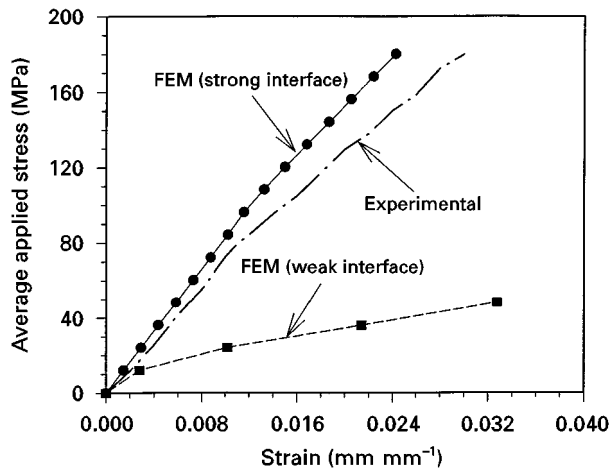


*Figure 4* Stress-strain plot at RT (without residual stress).

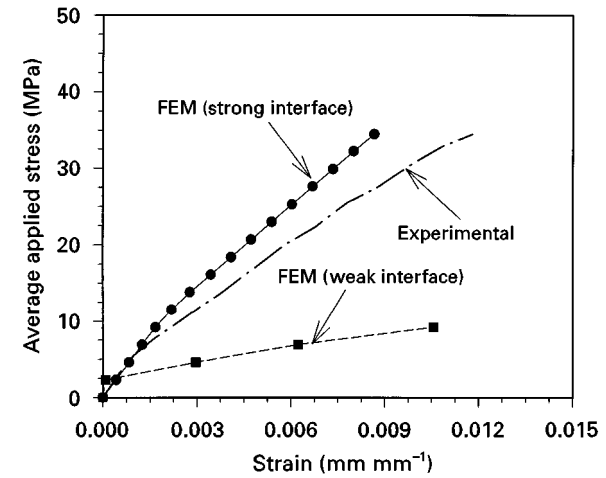


*Figure 5* Stress–strain plot at 1600 °C (without residual stress).

respectively. Both the contours are plotted at failure loads obtained from experimental data. It is observed that the fibres are undergoing compressive stress even though tensile stress is being applied to the unit cell. If we look at the nodes 122, 123, 222, 223, 227, 239 and 139 of Fig. 3b, all of which are on the upper region of the fibre, they have negative displacements in the $X$-direction. However, as we move towards the interface and to the region of the matrix, we see positive $X$-displacements. The magnitude of these displacements also increases as one moves to the matrix away from the interface. These positive $X$-displacements are much higher, sometimes of the order of 2, than the negative displacements. The physical rationale for such behaviour is attributed to the difference of stiffnesses of the matrix and the fibre. This causes significantly higher displacement of the main body of the matrix in the region between the two fibres. On the other hand, the $X$-displacements of the matrix in the neighbourhood of the interface are relatively smaller. This can be visualized as rotation of the matrix as a whole, which can cause negative displacement and eventually compressive stress on the upper region of the fibre. It is observed that the location of maximum tensile stress in Figs 6 and 7 is near the interface of 0° fibres. The difference between the two figures, besides temperature, is that some medium level stress is developed beyond the interface at RT, and this stress is somewhat relieved at higher temperature. The stress developed near the interface, as predicted by FEM, can cause the fibre–matrix interfacial failure in the form of fibre pull-out during failure. Because the fibre–matrix interface is strongly bonded in the present case, no fibre–matrix separation near the 90° fibre is observed.

Colour plots of $\sigma_x$ at RT and 1600 °C with weak interfaces are presented in Figs 8 and 9. The interface opening near the 90° fibre and interface slippage near the 0° fibre can be observed in Fig. 8. The location of maximum stress (at RT) is in the matrix near the loading surface which, however, shifts with the increase in temperature. It is also observed in Fig. 8 that compressive stress has developed in the 90° fibres due to the opening of the interface. At 1600 °C, as shown in Fig. 9, the compressive stress is maximum near the 0° interface. Matrix material has lower stiffness and strength than fibre material. This causes the matrix to be stretched more than the fibre, resulting in the failure of matrix prior to the fibre failure. As is known, the fibres then carry the load and fail in the form of fibre pull-out. In the fibre pull-out mechanism, fibre–matrix slippage, which, in turn, depends on interface strength, is important. This slippage phenomenon is clear in both Figs 8 and 9 where fibre–matrix separation is observed along the interface of 0° fibres. However, slippage along the layer separation plane is seen to be negligible because the matrices on both sides of this plane deform almost equally. It is also noticed in Fig. 9 that there is no opening of the interface near the 90° fibre as was observed at RT. Thermal expansion of the matrix at 1600 °C seems to have compensated for the gap created by the traction.

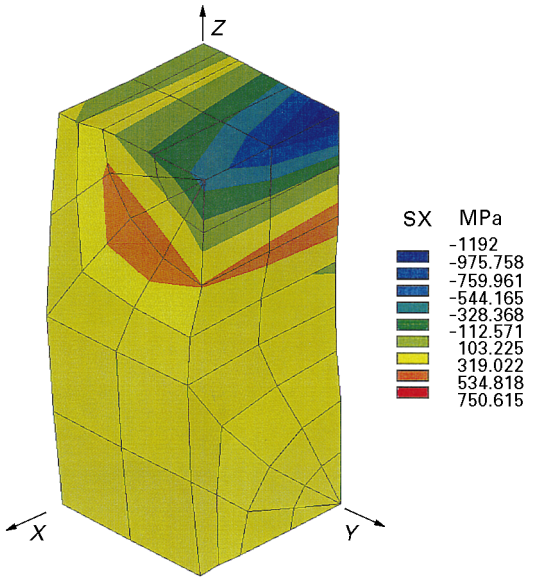


*Figure 6* Stress contour at room temperature for strong interface (without residual stress).

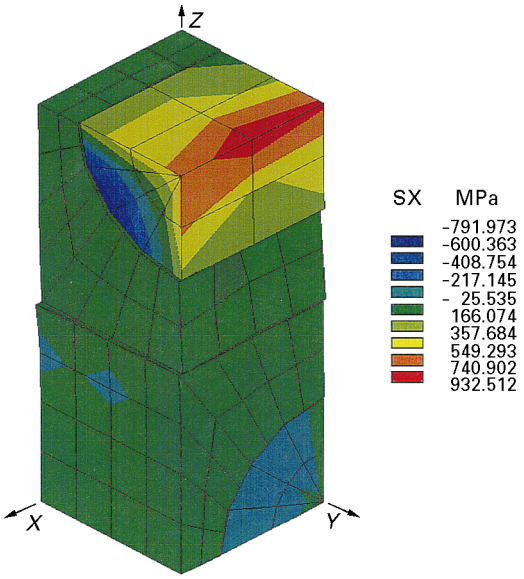


*Figure 9* Stress contour at 1600 °C for weak interface (without residual stress).

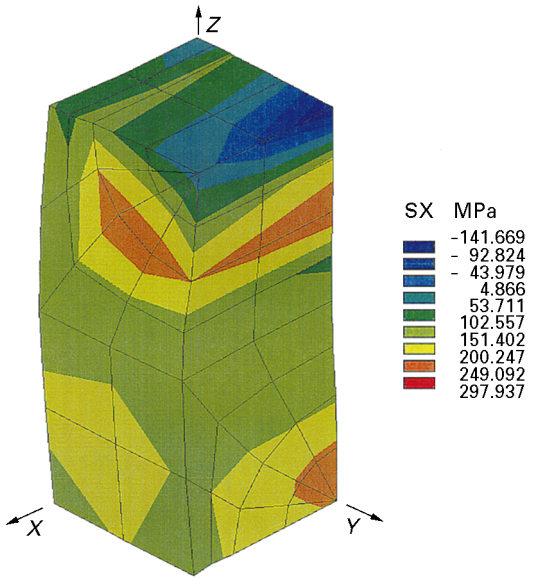


*Figure 7* Stress contour at 800 °C for strong interface (without residual stress).

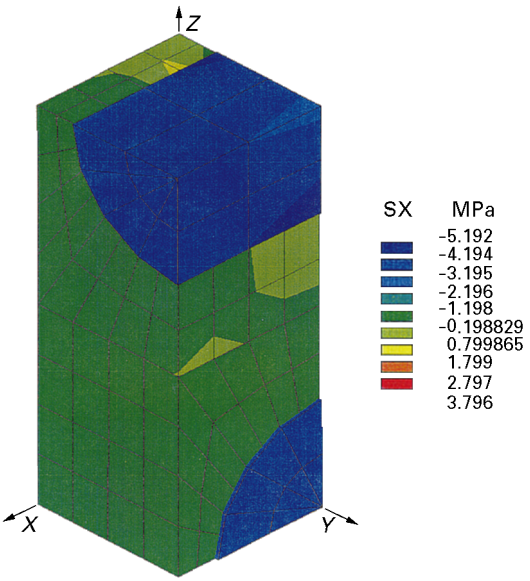


*Figure 10* $\sigma_x$ distribution due to thermal load only (weak interface).

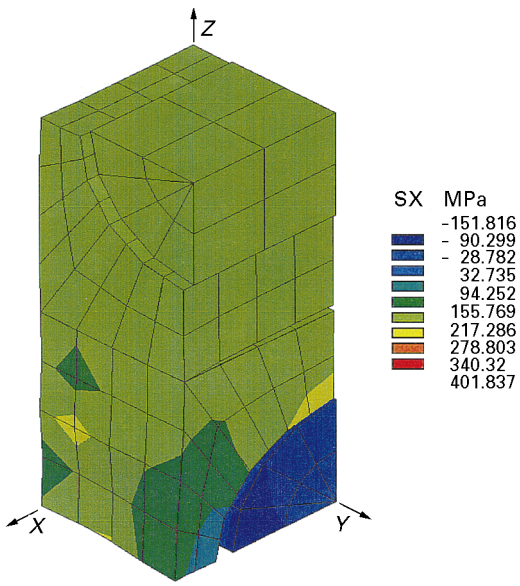


*Figure 8* Stress contour at room temperature for weak interface (without residual stress).

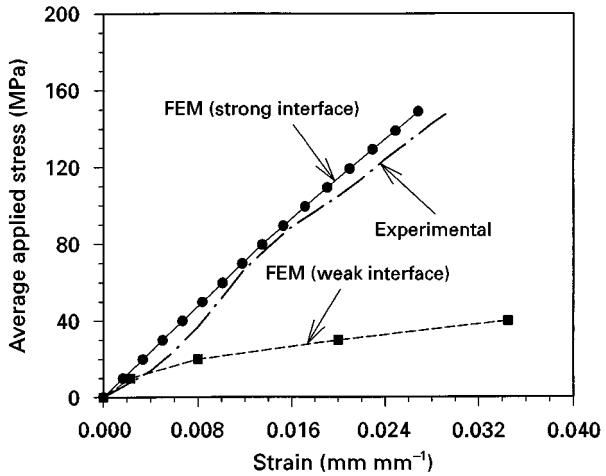


*Figure 11* Stress–strain plot at 800 °C (with residual stress).

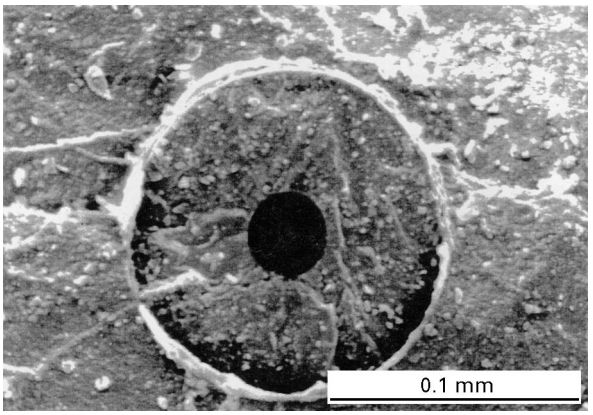


*Figure 13* SEM micrograph at 800 °C.

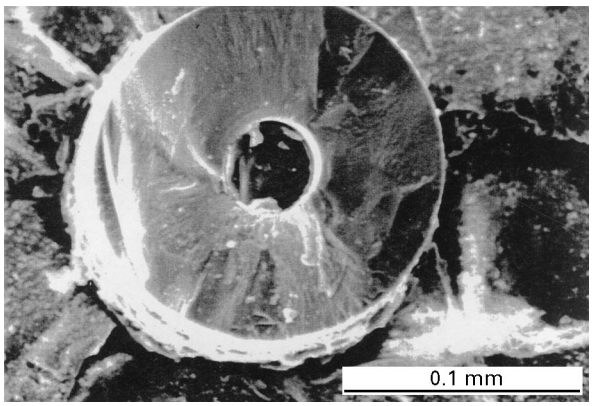


*Figure 12* SEM micrograph at room temperature.

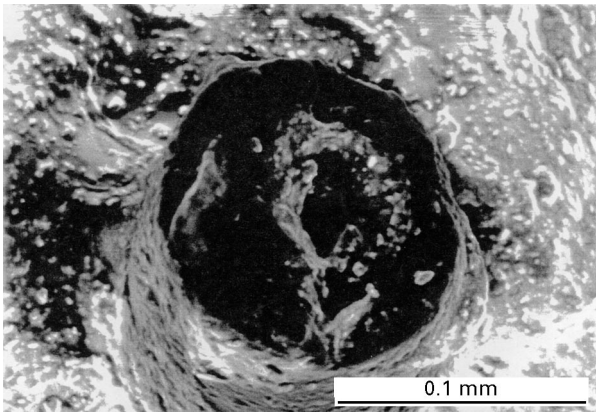


*Figure 14* SEM micrograph at 1600 °C.

## 4.2. With residual stress

First, the state of stress induced by the cooling process from 1700 °C to 23 °C has been considered in the model. Fig. 10 shows the distribution of $\sigma_x$ due to this thermal load for the weak interface condition. It is observed in Fig. 10 that both 0° and 90° fibres are uniformly stressed and the stress is compressive. This compressive stress in the fibre is typical in a situation where there is residual stress and the cause of such stress is the thermal expansion mismatch between the fibre and the matrix. Although the fibres are uniformly stressed, there are pockets of low-level stress in the body of the matrix near the layer separation plane and near the 0° fibre. Other than this, the bulk of the matrix is under compressive stress. The magnitude of this stress is, however, less than that of the fibre. The overwhelming presence of compressive stress is due to the fact that the cooling down process from 1700 °C to 23 °C has caused the overall contraction of the unit cell.

In the next step, load is applied in the longitudinal direction ($X$-direction) after the cool-down process. Fig. 11 illustrates the average stress–strain response of the unit cell at 800 °C. The zero reference state for the strain in Fig. 11 is considered to be the composite strain after cool down. The correlation between experimental and FEM, as shown in Fig. 11, is better for the strong interface as was observed previously. However, it may be noted that the initial modulus for both strong and weak interfaces matches closely with experiment. For the weak interface, the composite with a compressive residual stress at the interface will behave as a composite with finite interface strength until the compressive residual stresses are overcome by the tensile mechanical load. Once the residual stresses are overcome, the addition of external tensile load will cause fibre–matrix separation along the interface of 90° fibre. This separation results in more longitudinal displacement of the unit cell with a weak interface condition, as opposed to that with a strong interface. This higher displacement in the case of the weak interface, is the reason for the lower modulus after the initial loading, as seen in Fig. 11.

## 4.3. SEM

Figures 12–14 show scanning electron micrographs of the fractured specimens at RT, 800 and 1600 °C, respectively. The RT-tested specimens failed predominantly by brittle fracture, accompanied by pronounced separation of fibre–matrix interface (Fig. 12). This interface separation along 0° fibres is clear for the weak interface model, and has been explained earlier (Fig. 8). For the strong interface model, this separation is not visualized due to the sharing of a common node by both fibre and matrix. However, it

was observed in Fig. 6 that maximum tensile stress, $\sigma_x$, did develop at the interface of the 0° fibre. Now, if the interface strength is not sufficient to withstand the applied stress, the final failure will take place by fibre pull-out in the $X$-direction. Thus interface debonding will take place, as is seen in Fig. 12.

Failure of the specimens tested at 800 °C resembled closely the brittle fracture of the RT-tested specimens. The extent of the fibre–matrix interface separation was considerably less (Fig. 13) at 800 °C, and the failure was catastrophic. SiC fibre features a double carbon-rich layer on the outside surface. The purpose of this double carbon layer is to enhance the intrinsic strength of the fibre and also to provide a debonding mechanism between the matrix and fibre to increase the fracture toughness of the composite. At high temperature, the reaction between this carbon and atmospheric oxygen reduces the amount of carbon outside the fibre thereby reducing the debonding between fibre and matrix.

A drastic difference in failure was observed for the 1600 °C-tested composites. There was ample evidence of oxidation of the $Si_3N_4$ matrix at this temperature. The amount of matrix adhering to the fibre surfaces following fracture was much higher (Fig. 14) than either of the previous cases. The progressive failure of composites tested at 1600 °C is primarily due to the weakening of the $Si_3N_4$ matrix and deformation of the fibre core at that temperature range.

## 5. Conclusions

1. A three-dimensional unit cell has been developed and incorporated into an FEM programme which can be used for [0°/90°] laminated composites.

2. Ceramic matrix composites, namely $SiC_f/Si_3N_4$, has been investigated with this model and reasonably good correlation with the experimental stress–strain curves has been established.

3. Between the two interface conditions, namely strong and weak, the strong interface has been observed to agree well the experimental data.

4. It has been observed that unidirectional fibres experience higher stress than the matrix. For a strong interface condition, a considerable amount of stress is developed near the interface which is higher than the matrix yield strength. This stress can cause localized interfacial failure ahead of the ultimate failure of the laminate.

5. Finally, a finite element technique using gap elements has been established to study the interface behaviour of cross-ply laminates of single fibre composites.

## Acknowledgements

The authors thank the National Science Foundation (NSF) for support under Grant HRD-9653068.

## References

1. H. MAHFUZ, U. VAIDYA, M. MANIRUZZAMAN, T. BROWN and S. JEELANI, in "19th Annual Conference, American Ceramic Society (ACerS)", edited by J. B. Wachma Vol. 16, No. 4 (1995) pp. 351–60, Westerville, Ohio 43081.
2. C. Q. ROUSSEAU, in "Thermal and Mechanical Behavior of Metal Matrix and Ceramic Matrix Composites", ASTM STP 1080, edited by J. M. Kennedy, H. H. Moeller and W. S. Johnson (American Society of Testing and Materials, Philadelphia, PA, 1990) pp. 136–51.
3. JOHN J. PETEROVIC and GEORGE F. HURLEY, "Fiber Reinforced Ceramic Composites", edited by K. S. Mazdiyasni (Noyes, Publications 1990, NJ) pp. 93–121.
4. RONALD J. KERANS, RANDALL S. HAY and NICHOLAS J. PAGANO, *Am. Ceram. Soc. Ceram. Bull.* **68** (1989) 429.
5. MILIVOJ K. BRUN, *J. Am. Ceram. Soc.* **75** (1992) 1914.
6. W. WARREN (Ed.), "Ceramic Matrix Composites" (Chapman and Hall, New York, NY, 1992) pp. 64–111.
7. D. C. CRANMER, U. V. DESHMUKH and T. W. COYLE, in "Thermal and Mechanical Behavior of Metal Matrix and Ceramic Matrix Composites", ASTM STP 1080, edited by J. M. Kennedy, H. H. Moeller and W. S. Johnson (American Society of Testing and Materials, Philadelphia, PA, 1990) pp. 124–135.
8. H. MAHFUZ, A. K. M. A. MIAN, U. K. VAIDYA, T. D. BROWN and S. JEELANI, in "MRS Fall Meeting", Materials Research Society Symposium Proceedings, (eds) Richard A. Lorrden, Pittsburgh, PA, Materials Research Society, Vol. 365 (MRS, 1994) pp. 229–36.
9. E. S. FOLIAS, *J. Compos. Mater.* **25** (1991) 869.
10. H. MAHFUZ, D. XUE and S. JEELANI, *Compos. Sci. Technol.* **50** (1994) 411.
11. P. PLUVINAGE and J. M. QUENISSET, *J. Compos. Mater.* **27**(2) (1993) 153.
12. B. G. SCHAFFER and D. F. ADAMS, *J. Appl. Mech.* **48** (1981) 859.
13. I. CARTIAN and RONALD F. GIBSON, in NCA-Vol. 18/DE-Vol. 80, "Materials for Noise and Vibration Control", (Eds) P. K. Raju and Ronald F. Gibson (ASME, 1994) pp. 73–86.
14. RONALD P. NIMMER, *J. Compos. Technol. Res.* **12** (2) (1990) 65.
15. RONALD P. NIMMER, R. J. BANKERT, EDWARD S. RUSSEL, GARY A. SMITH and KENNARD P. WRIGHT, *J. Compos. Technol. Res.* **13** (1) (1991) 3.
16. G. L. POVIRK and A. NEEDLEMAN, *J. Eng. Mater. Technol.* **115** (1993) 286.
17. P. KOHNKE, "ANSYS Engineering Analysis Systems- Theoretical Manual", (Swanson Analysis Systems, Houston, PA, 1992).
18. R. D. COOK, "Concepts and Applications of Finite Element Analysis", 2nd Edn (Wiley, New York, 1981).
19. O. C. ZIENKIEWICZ and R. L. TAYLOR, "The Finite Element Method", 4th Edn, Vol. 1 (McGraw-Hill, New York, NY, 1989).
20. A. L. HIGHSMITH, D. SHIN and R. A. NAIK, in "Thermal and Mechanical Behavior of Metal Matrix and Ceramic Matrix Composites", ASTM STP 1080, edited by J. M. Kennedy, H. H. Moeller and W. S. Johnson (American Society of Testing Materials, Philadelphia, PA, 1990) pp. 3–19.

*Received 23 April 1996*
*and accepted 13 February 1998*